RSC Advances

PAPER

View Article Online
View Journal | View Issue

Cite this: *RSC Adv.*, 2024, **14**, 1267

Pressure-induced tuning of physical properties in high-throughput metal halide MSn_2Br_5 ($M = K, Cs$) perovskites for optoelectronic applications†

Md. Khairul Alam, Md. Nadim Mahamud Nobin and Md. Lokman Ali *

Received 12th September 2023
Accepted 19th December 2023

DOI: 10.1039/d3ra06215e

rsc.li/rsc-advances

The physical properties of the ferromagnetic oxide perovskites MSn_2Br_5 ($M = K, Cs$) were thoroughly examined using the GGA + PBE formalism of density functional theory. The investigation includes a comprehensive characterization of these materials under hydrostatic pressures ranging up to 25 GPa. Our work represents the first theoretical framework for exploring the behavior of MSn_2Br_5 ($M = K, Cs$) under pressure, providing valuable insights into their properties. To ensure the thermodynamic and mechanical stability of the studied compounds, we justified their stability through the analysis of formation energy and Born stability criteria. Furthermore, we conducted a thorough examination of the mechanical features of MSn_2Br_5 ($M = K, Cs$) based on various parameters, such as elastic constants, elastic moduli, the Kleinman parameter, the machinability index, and the Vickers hardness. Pugh's ratio and Poisson's ratio data show a ductile behavior for both compounds under stress. Moreover, our analysis of the refractive index suggests that both materials hold significant potential as candidates for ultrahigh-density optical data storage devices, particularly when subjected to appropriate laser irradiation. This finding opens up exciting possibilities for utilizing MSn_2Br_5 ($M = K, Cs$) in advanced optical technologies.

1. Introduction

The multifunctional optical properties of perovskite materials are currently attracting significant attention in the field of optoelectronic applications.[1–3] Nevertheless, the potential toxicity associated with the presence of lead in these compounds has generated significant concerns.[4,5] Consequently, there has been a notable increase in interest within the scientific field regarding lead-free halide perovskites.[6–9] Researchers have conducted investigations into a range of physical features exhibited by these materials, encompassing structural, electrical, optical, and mechanical attributes. The goals of these efforts are to increase our understanding and overcome the challenges associated with their practical use. The physical properties of a material, and hence its potential uses, are often analyzed using both experimental and theoretical methods.[10–13] The arrangement of atoms within a material can significantly affect its physical characteristics. Perovskite materials encompass a wide range of properties, such as conductivity, insulation, semi-conduction, and superconductivity.[14,15] Consequently, perovskites are widely recognized as a highly significant group of materials encompassing different crystal forms.[16]

The perovskite groups exhibits a diverse array of physical characteristics such as photocatalysis, dielectric behavior, ferroelectricity, pyroelectricity, piezoelectricity, magnetism, superconductivity, and ionic conductivity.[17–19] Researchers have used first-principles simulations to investigate and learn about the various physical features of cubic perovskite materials.[20–24] Chemical alterations, atomic substitutions, metal doping, hydrostatic pressure, electric fields, and magnetic fields are only a few of the methods used to alter the physical features of materials. Among these approaches, applying external hydrostatic pressure stands out as a convenient and highly effective method for altering the band gap of perovskite materials.[25] This modification, in turn, significantly influences their optical and electronic properties.

In recent advancements, researchers have made major advances in enhancing the efficacy of cesium lead halide (CsPbX) perovskite solar panels, resulting in power conversion efficiencies (PCE) that exceed 20%.[26] In order to address environmental concerns, various alternative compounds such as Sn^{2+}, Ge^{2+}, Bi^{3+}, and Sb^{3+} have been explored to replace the hazardous Pb^{2+}.[27] Among these alternatives, tin (Sn^{2+}) is regarded as a particularly captivating substance due to its perceived environmentally friendly nature. As a result, solar cells, photodetectors, and LEDs made from tin-based organic–inorganic

---

Department of Physics, Pabna University of Science and Technology, Pabna-6600, Bangladesh. E-mail: lokman.cu12@gmail.com

† Electronic supplementary information (ESI) available. See DOI: https://doi.org/10.1039/d3ra06215e

halide perovskites (OIHPs) have demonstrated outstanding prospects as lead-free materials.[28]

Extensive research on Sn-based OIHPs with different halide anions (I^-, Br^-, and Cl^-) has been published, with a particular focus on their application in solar cells. Perovskite structures are typically represented by general formulas such as ABX_3, AB_2BX_4, AB_2BX_5, and A_4BX_6, where A stands for organic or inorganic cation (such as CH_3NH^{2+}, Cs^+, or Rb^+), B denotes a metal cation (such as Pb^{2+}, Sn^{2+}, Ge^{2+}, Bi^{3+}, or Sb^{3+}), and X signifies a halide anion (I^-, Br^-, or Cl^-).[29] Nevertheless, there remains a need for further technological advancements for making perovskites without using lead to enable their widespread utilization in various applications. Researchers have reported a technique for the facile and composition-dependent synthesis of AB_2X_5 perovskites.[30–32] Compared to other perovskite systems such as ABX_3, AB_2BX_4, and A_4BX_6, AB_2X_5 perovskites have been noted for their superior structural stability.[33–35] Several studies have investigated the optoelectronic characteristics of specific AB_2X_5 perovskite compositions, such as $CsSn_2Br_5$ and $CsSn_2Cl_5$.[36,37]

A detailed examination was carried out to examine the effects of pressure on (metal) halide perovskites through the utilization of density functional theory (DFT) computations. The main aim of our study was to improve the efficiency of solar cells and other electronic equipment with a comprehensive investigation of the impact of pressure on diverse physical characteristics. In accordance with limited research performed in this field, our investigation utilized first-principles simulations to examine the response of (metal) halide perovskites to varying levels of pressure. Our study focused on the halide based MSn_2Br_5 (M = K, Cs) perovskites. We conducted an investigation on the perovskites, examining alterations in their structural, mechanical, electrical, optical, and thermodynamic characteristics by subjecting them to pressures which varied from 0 to 25 GPa. In terms of structural properties, we examined lattice parameters, volume, and formation energy. The elastic properties of perovskite materials were performing by estimations several parameters including elastic constants, Young's modulus, bulk modulus, shearing modulus, Pugh's ratio, Poisson's ratio, Kleinman parameter, machinability index, anisotropy, and Vickers hardness. The evaluation of electronic qualities involved the examination of band structures, total and partial density of states (TDOS and PDOS). On the other hand, the analysis of optical properties involved several factors such as reflectivity, conductivity, dielectric functions, absorption coefficient, loss functions, and refractive index. Furthermore, we investigated thermodynamic characteristics, with an emphasis on the Debye temperature. Our findings revealed a unique band structure and significant alterations in reflectivity, loss functions, absorption coefficient, and conductivity, particularly in the ultraviolet region, as pressure was applied within the range of 0 to 25 GPa. Notably, we observed noticeable elastic behaviors in the perovskite materials. Based on the distinctive optical characteristics identified in MSn_2Br_5 (M = K, Cs), we suggest that this material could be used in high-density optical data store systems.

2. Computational method

In this investigation, we used the CASTEP algorithm to carry out first principles calculations that rely on Density Functional Theory (DFT).[38,39] To explain the exchange–correlation energies, the GGA approximation, specifically a simplified form of Perdew–Burke–Ernzerhof (PBE), was used.[40] The simulations involved using pseudo-atomic models to consider the valence electrons. In this investigation, the valence electron configurations of the MSn_2Br_5 (M = K, Cs) compound are as follows: K-$3p^6$ $4s^1$, Cs-$5p^6$ $6s^1$, Sn-$5s^2$ $5p^2$, and Br-$3d^{10}$ $4p^5$. To achieve the most favorable structure and calculate the total energy, a plane wave cut-off energy of 520 eV was determined, while the *k*-point was set at $4 \times 4 \times 3$ using the Monkhorst–Pack approach, ensuring the *k*-points fell within the Brillouin zone.[41] The optimal structure was obtained using the Broyden–Fletcher–Goldfarb–Shanno (BFGS) method.[42] For geometry optimization, the convergence tolerance factors were established as follows: 1×10^{-5} eV Å^{-1} atom for total energy, 1×10^{-3} Å for maximum displacement, 0.03 eV Å^{-1} for maximum force, and 0.05 GPa for maximum stress. During structural optimization, the hydrostatic pressure was raised from 0 to 25 GPa in 5 GPa increments. The optimal crystal structure was generated using the VESTA programme.[43] In the same way that structural optimization criteria were used, so too were electrical and optical qualities. Elastic moduli and constants were calculated with the CASTEP algorithm's "stress–strain" approach.[44] In addition, anisotropic contour plots in three dimensions (3D) were created for Young's modulus, shear modulus, Poisson's ratio, and linear compressibility using the ELATE programme.[45]

3. Results and discussion

3.1 Structural characteristics

The materials under investigation exhibit a tetragonal crystal structure, which crystalizes in the point group 4/*mm* (140) and space group *I*4/*mcm*.[46] Fig. 1 displays the optimized crystal structures of MSn_2Br_5 (M = K, Cs). Using fractional coordinates, the K atoms in KSn_2Br_5 are found at the 4a Wyckoff position (1/2, 1/2, 1/4), the Sn atoms at the 8h Wyckoff position (0.18, 0.68, 0.5), and the Br atoms at the 3d Wyckoff position (0.0, 0.0, 1/2). Similarly, in $CsSn_2Br_5$, Cs atoms are found in the 4a Wyckoff position with fractional coordinates of (0, 0, 1/4), while Sn atoms occupy the 8h Wyckoff site with fractional coordinates of (0.18, 0.68, 1/2), and Br atoms are located in the 4c Wyckoff position with fractional coordinates of (1/2, 1/2, 0). Fig. 2 shows that at normal atmospheric pressure, the predicted lattice constants of KSn_2Br_5 is 8.39 Å ($a = b$) and 14.99 Å, which is quite close to the value given in the reference work, 8.36 Å and 14.46 Å.[46] The lattice constant for $CsSn_2Br_5$ is 8.54 Å ($a = b$) and 16.15 Å, which is nearly close to the value found in the earlier work 8.48 Å ($a = b$) and 15.28 Å.[47] Hydrostatic pressure is applied between 0 and 25 GPa to both compounds. The structural properties are significantly affected through the utilization of pressure. Fig. 2 and 3 demonstrate how the lattice constants and formation energy are affected by hydrostatic pressure. The declining lattice constants are graphically represented. In the meantime, it was evident from Table S1† that the volume of

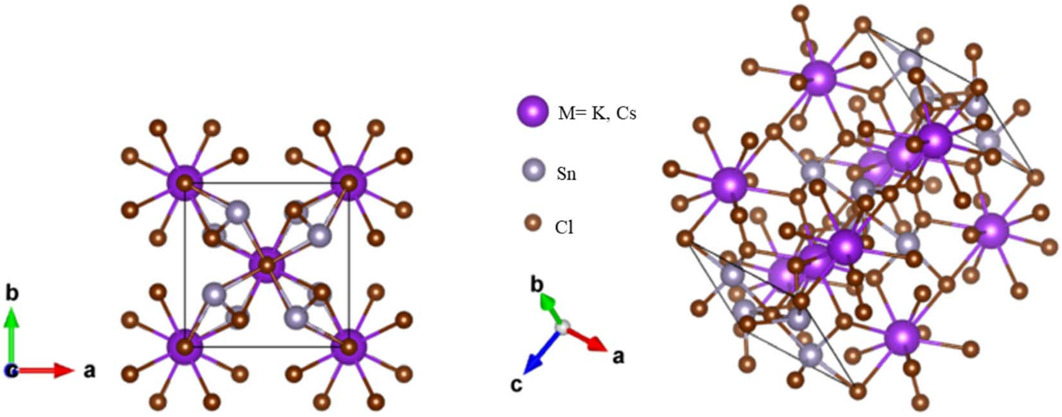

Fig. 1 The 2D and 3D crystal structures of MSn_2Br_5 (M = K, Cs) perovskites.

both compounds was decreasing, which indicates that bond length decreases as pressure is applied. The formation energy (ΔE_f) is calculated using the following equation to ensure the phase stability of MSn_2Br_5 (M = K, Cs) under pressure:[48]

$$\Delta E_f(MSn_2Br_5) = E_{total}(MSn_2Br_5) - E_{solid}(M) - 2E_{solid}(Sn) - \frac{5}{2}E_{solid}(Br_2)$$

where, $E_{total}(MSn_2Br_5)$ = total energy of the bulk MSn_2Br_5 system per formula unit, $E_{solid}(M)$ and $E_{solid}(Sn)$ are the total energy of the bulk M atom and bulk Sn atom per formula unit, and $E_{solid}(Br_2)$ = total energy of the bromine molecule per formula unit. A material must have a negative formation energy for thermodynamic stability.[49] Thermodynamic stability of MSn_2Br_5 (M = K, Cs) perovskites is indicated by negative values of ΔE_f at all applied pressures.

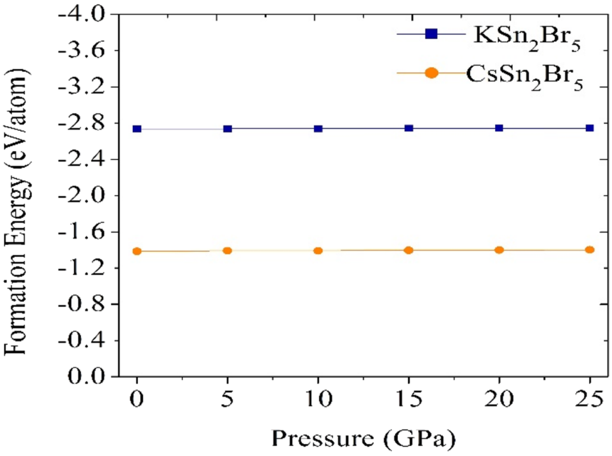

Fig. 3 Influence of pressure on formation energy of MSn_2Br_5 (M = K, Sn) perovskites.

The formability of metal halide perovskites depends on various requirements. The Goldschmidt tolerance factor t is one of them. We calculated the Goldschmidt tolerance factor t of the studied compounds by using the following equation,

$$t = \frac{(r_A + r_X)}{\sqrt{2}(r_B + r_X)}$$

where r_A and r_B are the ionic radii of A and B site cations and r_X is the ionic radii of the anion. The calculated value of t for KSn_2Br_5 and $CsSn_2Br_5$ is 0.831 and 0.887, respectively. It has been well accepted that the ideal tolerance factor of ternary

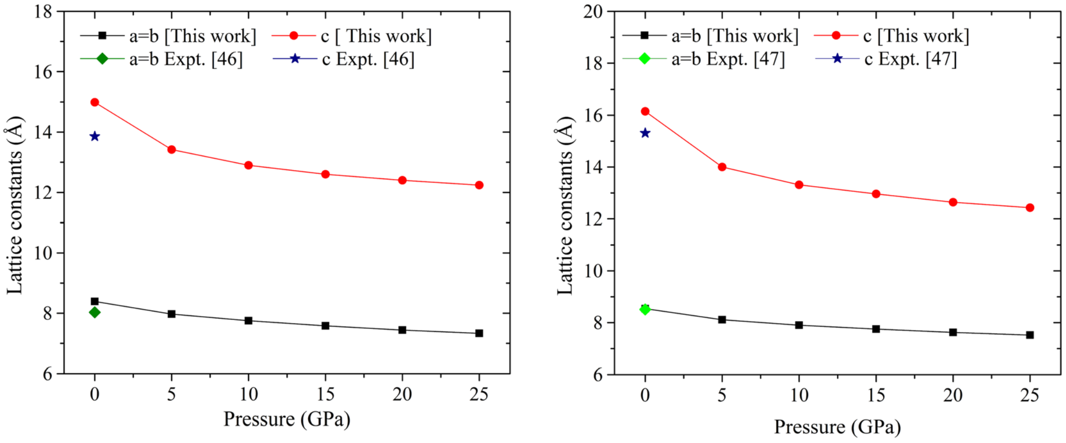

Fig. 2 Pressure effect on lattice constants of (a) KSn_2Br_5 and (b) $CsSn_2Br_5$ perovskites.

halide perovskites ranges from 0.813 to 1.107.[50] Therefore, the calculated value of t indicates their structural stability. Again, the tolerance factor falls between the range ($t = 0.80$–0.89), which suggests that the studied compounds should form distorted perovskite structures with more likely orthorhombic, tetragonal, or rhombohedral crystal structures.

3.2 Elastic constants

Elastic constants C_{ij} have a major role in determining a material's structural stability and mechanical qualities.[51] These numbers describe how far a substance changes shape under force and then goes back to its original shape when the force is removed. It can be used to investigate the anisotropy, ductility, stability, brittleness, and stiffness of a material. In this section, we will take a close look at the elastic properties of MSn_2Br_5 (M = K, Cs) perovskite materials. We determined the elastic constants required by Hook's law using a linear fit stress–strain technique.[52]

Six different elastic constants (C_{11}, C_{12}, C_{13}, C_{33}, C_{44}, and C_{66}) are associated with a tetragonal crystal structure. The directionality of stress and strain are revealed by the values of these elastic constants. They play a crucial role in determining how different materials will react to mechanical stress. The stiffness in the axial direction is described by the constants C_{11}, C_{12}, and C_{13}, and the stiffness in the perpendicular direction is described by the constant C_{33}. Shear stiffness along a plane perpendicular to the axis is described by the C_{66} constant, and along a plane parallel to the axis, by the C_{44} constant. The following Born stability criteria must be satisfied for elastic constants in a tetragonal structure to be regarded as stable:[53]

$$C_{11} > 0,\ C_{33} > 0,\ C_{44} > 0,\ C_{66} > 0,\ C_{11} + C_{33} - 2C_{13} > 0,\ C_{11} - C_{12} > 0,\ 2(C_{11} + C_{12}) + C_{33} + 4C_{13} > 0.$$

In this instance, the crystal structure under study is mechanically stable. Since our evaluation of the MSn_2Br_5 compound's six elastic constants satisfied these stability requirements, the compound is stable. This investigation indicates that the bulk modulus B must satisfy the quality conditions $C_{12} < B < C_{11}$. The main objective of this study is to demonstrate the effect of pressure on the elastic constants of MSn_2Br_5 (M = K, Cs) perovskites. Fig. 4 illustrates that the elastic constants exhibit a rising pattern as the exerted pressures enhance, so suggesting a concurrent augmentation in the crystal's stiffness and resistance to deformation. The present findings can be considered to be predictive research due to the absence of any experimental or theoretical data regarding the elastic constants (C_{ij}) of MSn_2Br_5 substance at high-pressure conditions.

3.3 Mechanical properties

The computed elastic constants are useful as an initial reference for estimating these characteristics using the Voigt–Reuss–Hill averaging technique.[54] The ability of a substance to endure plastic deformation when subjected to hydrostatic pressure and shear stress can be quantified by its bulk modulus (B) and shear modulus (G), respectively.[55] The increase in pressure is accompanied by a rise in both the shear modulus and the bulk modulus as depicted in Fig. 5. The findings indicate that the tetragonal crystal MSn_2Br_5 (where M represents either K or Cs atom) has enhanced resistance to compression under elevated pressures. Further, it is demonstrated that the influence of pressure on the bulk modulus is more significant compared to its impact on the shear modulus. The Young's modulus is a fundamental mechanical parameter that characterizes the stiffness of materials. The concept of tensile stress can be defined as the ratio of stress to strain.[56] The relationship between rough stiffness and a high Young's modulus is a widely accepted characteristic among scientists. As depicted in Fig. 5, the computed Young's modulus (E) values for MSn_2Br_5 perovskites exhibit an upward trend as pressure is elevated, suggesting that pressure exerts a significant influence on their durability.

The evaluation of the ductility of a substance or fragility can be conducted by an investigation of its Pugh's ratio. Fig. 6(a) presents the Pugh's ratio for MSn_2Br_5 (M = K, Cs) perovskites. This ratio is calculated by dividing the bulk modulus by the

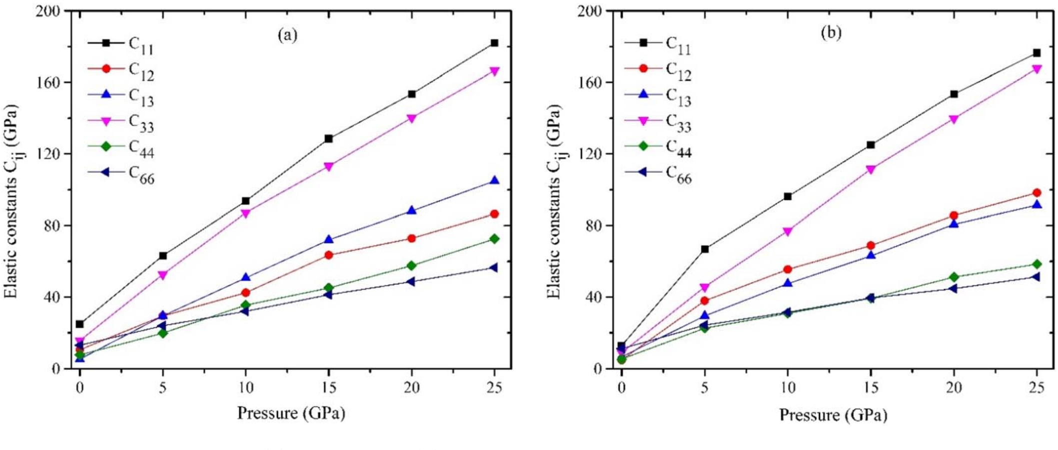

Fig. 4 Variation of elastic constants C_{ij} for (a) KSn_2Br_5 and (b) $CsSn_2Br_5$ perovskites.

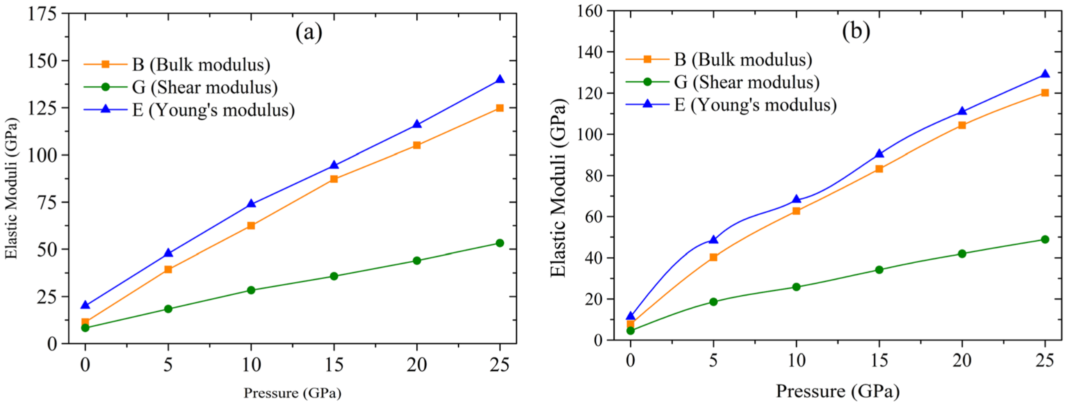

Fig. 5 Effect of pressure on elastic moduli of (a) KSn_2Br_5 and (b) $CsSn_2Br_5$ perovskites.

shear modulus. Pugh's ratio asserts that the character of a solid is connected to its B/G value,[57] with a small (large) B/G value indicating a brittle (ductile) solid. This ratio is indicative of brittleness relative to ductility, with the latter being more easily distinguished when it is closer to 1.75. As can be seen in Fig. 6(a), the ratio of B/G increases with pressure. As an outcome, higher pressures result in more ductility in MSn_2Br_5 ($M = K$, Cs) perovskites. Another measure for assessing ductility is the Poisson's ratio, the critical value of which is 0.26. The ductility of MSn_2Br_5 ($M = K$, Cs) compounds is indicated by the fact that their predicted value of ν is greater than 0.26 for a wide range of stresses. Fig. 6(b) illustrates that as pressure is increased, the value of ν for both materials increases above 0.26. Consequently, this results in the perovskite material exhibiting increased ductility.

The hardness of a substance can be approximated using either the Vickers hardness (H_ν) or the macroscopic structures for durability estimation (E, G, B, ν, and G/B).[58] These can be used to express the relationships:[59]

$$H_1 = 0.0963B$$

$$H_2 = 0.0607E$$

$$H_3 = 0.1475G$$

$$H_4 = 0.0635E$$

$$H_5 = -2.899 + 0.1769G$$

$$H_6 = \frac{(1-2\nu)B}{6(1+\nu)}$$

$$H_7 = \frac{(1-2\nu)E}{6(1+\nu)}$$

$$H_8 = 2(k^2G)^{0.585} - 3$$

here, $k = \frac{B}{G}$ is Pugh's ratio.

The variation of hardness with pressure is depicted in Fig. 7(a) and (b), it clearly reveal that both compound's hardness value increase with increasing pressure. Based on the findings, the application of pressure causes complexities in both rigid and flexible deformation processes.

For tetragonal structure,

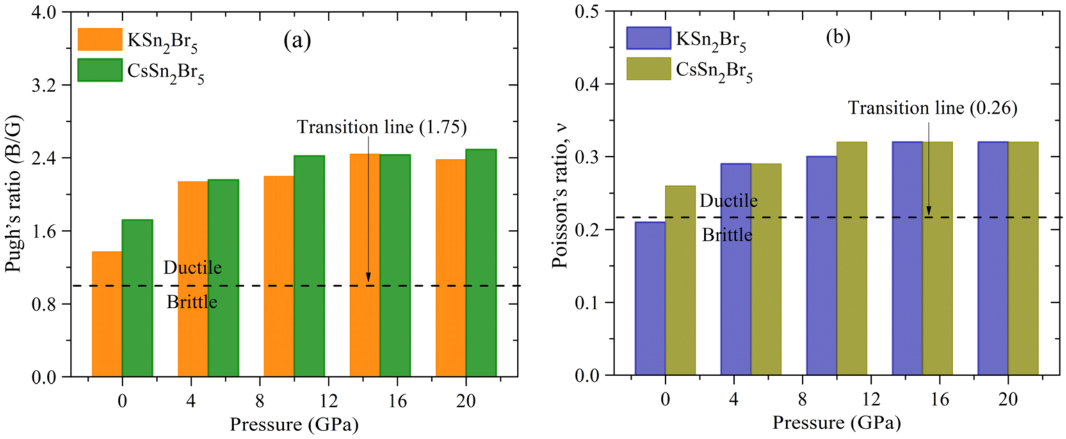

Fig. 6 Variation of pressure on (a) Pugh's ratio and (b) Poisson's ratio of MSn_2Br_5 ($M = K$, Cs) perovskites.

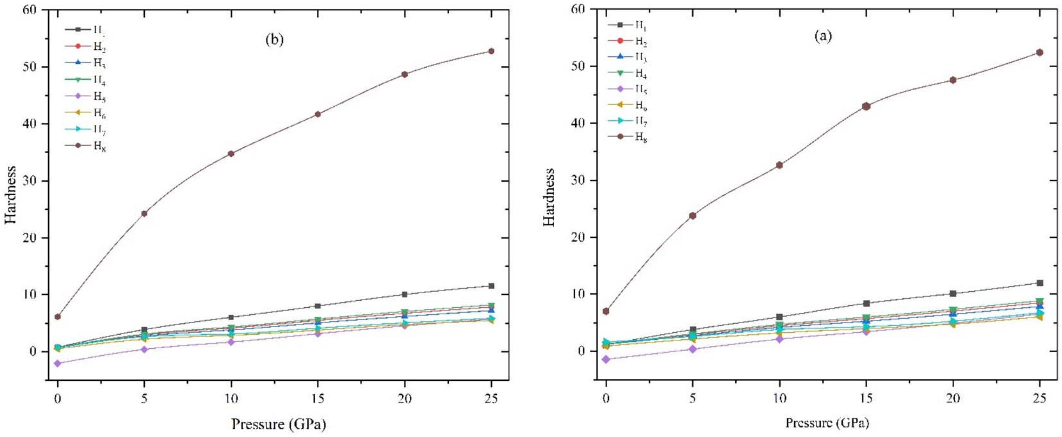

Fig. 7 Influence of pressure on hardness of (a) KSn_2Br_5 and (b) $CsSn_2Br_5$ perovskites.

$$A^{U} = 5\frac{G_{v}}{G_{R}} + \frac{B_{v}}{B_{R}} + 6 \geq 0$$

$$A^{G} = \frac{G_{v} - G_{R}}{G_{v} + G_{R}}$$

$$A^{B} = \frac{B_{V} - B_{R}}{B_{V} + B_{R}}$$

Therefore, A^{eq} is the equivalent Zener anisotropy factor, which can be written as:

$$A^{eq} = \left(1 + \frac{5}{12}A^{U}\right) + \sqrt{\left(1 + \frac{5}{12}A^{U}\right)^{2} - 1}$$

The standard log-Euclidean value can be mathematically expressed by utilizing the log-Euclidean formula, which is defined as follows:

$$A^{L} = \sqrt{\left[\ln\left(\frac{B_{V}}{B_{R}}\right)\right]^{2} + 5\left[\ln\left(\frac{C_{44}^{V}}{C_{44}^{R}}\right)\right]^{2}}$$

here, C_{44}^{v} and C_{44}^{R} represent the C_{44} values for Voigt and Reuss, respectively, which may be expressed as-

$$C_{44}^{R} = \frac{5}{3}\frac{C_{44}(C_{11} - C_{12})}{3(C_{11} - C_{12}) + 4C_{44}}$$

$$C_{44}^{V} = \frac{3}{5}\frac{(C_{11} - C_{12} - 2C_{44})^{2}}{3(C_{11} - C_{12}) + 4C_{44}}$$

The Kleinman parameter, denoted by the Greek letter ζ and having no units, is typically between zero and one. This index assesses the extent to which bonds can be extended in comparison to other types of assets. The strength of a substance to resist tension and compression is measured here. The following construction ζ can be used for a compound:[60]

$$\zeta = \frac{C_{11} + 8C_{12}}{7C_{11} + 2C_{12}}$$

Bond bending is minimized when ζ approaches zero, whereas bond stretching is minimized when ζ approaches one. The calculated value for ζ provides that this material exhibits bending-type bonding. Up to 25 GPa, the impact of pressure on the Kleinman parameter is seen in Tables 3 and 4. The machinability index, $\mu_{M} = B/C_{44}$, is a crucial efficiency metric with respect to future engineering applications. A solid's slicability is quantified by its μ_{M} value. Dry lubrication and adjustments become less complicated when μ_{M} is high.[61]

$$\mu_{M} = \frac{B_{H}}{C_{44}}$$

Tables 3 and 4 show the μ_{M} value of KSn_2Br_5 and $CsSn_2Br_5$ at different pressures, respectively; when pressure is increased this value increase up to around 15 GPa, but it begins to decline after that. Therefore, MSn_2Br_5 (M = K, Cs) perovskites become more amenable to machining at greater pressures. This means the compound can be machined with greater ease, less tool wear can be tolerated, the surface finish can be improved, productivity can rise, and new machining options can be explored. Tables 3 and 4 show the computed values of C_{44}, anisotropy, and different anisotropy factors for KSn_2Br_5 and $CsSn_2Br_5$ at different applied pressures. Anisotropy is indicated by a value of 0 for both A^{G} and A^{B}, while anisotropy is indicated by a value of 1. Since shear anisotropy is greater than compressibility anisotropy, our results show that MSn_2Br_5 (M = K, Cs) is anisotropic. In contrast to A^{U}, which measures relative anisotropy, A^{L} quantifies the absolute anisotropy of a crystalline solid. However, A^{U} does not provide any quantitative information about the extent of anisotropy exhibited by a material.

Three-dimensional changes in elastic moduli, compressibility β, and Poisson's ratio ν were visualized using the ELATE method.[62] The ELATE program displays the E, β, G, and ν and anisotropy values in MSn_2Br_5 (M = K, Cs) perovskites at either

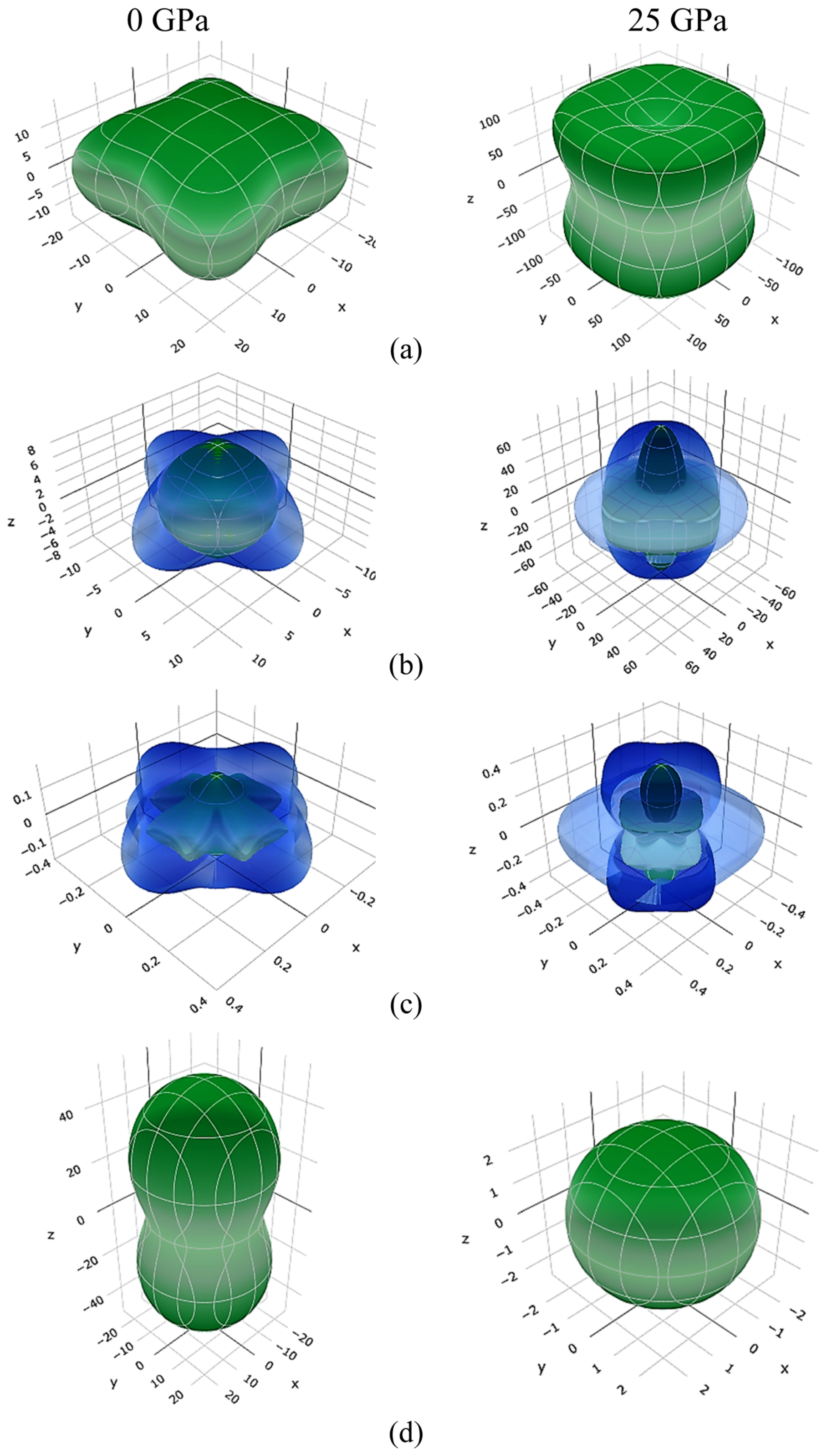

Fig. 8 Anisotropic three-dimensional depiction of (a) Young's modulus, (b) Shear modulus, and (c) Poisson's ratio (d) linear compressibility of KSn_2Br_5 perovskite at 0 and 25 GPa pressures.

0 or 25 GPa, determined using the provided matrix. Fig. 8 and 9 show how the elastic moduli changes along different directions. Three-dimensional (3D) sphere plots show isotropy, while non-sphere plots show anisotropy.[63] 3D contour plots that aren't spherical reveal the presence of elastic anisotropy in all directions in the MSn_2Br_5 perovskites under study. The

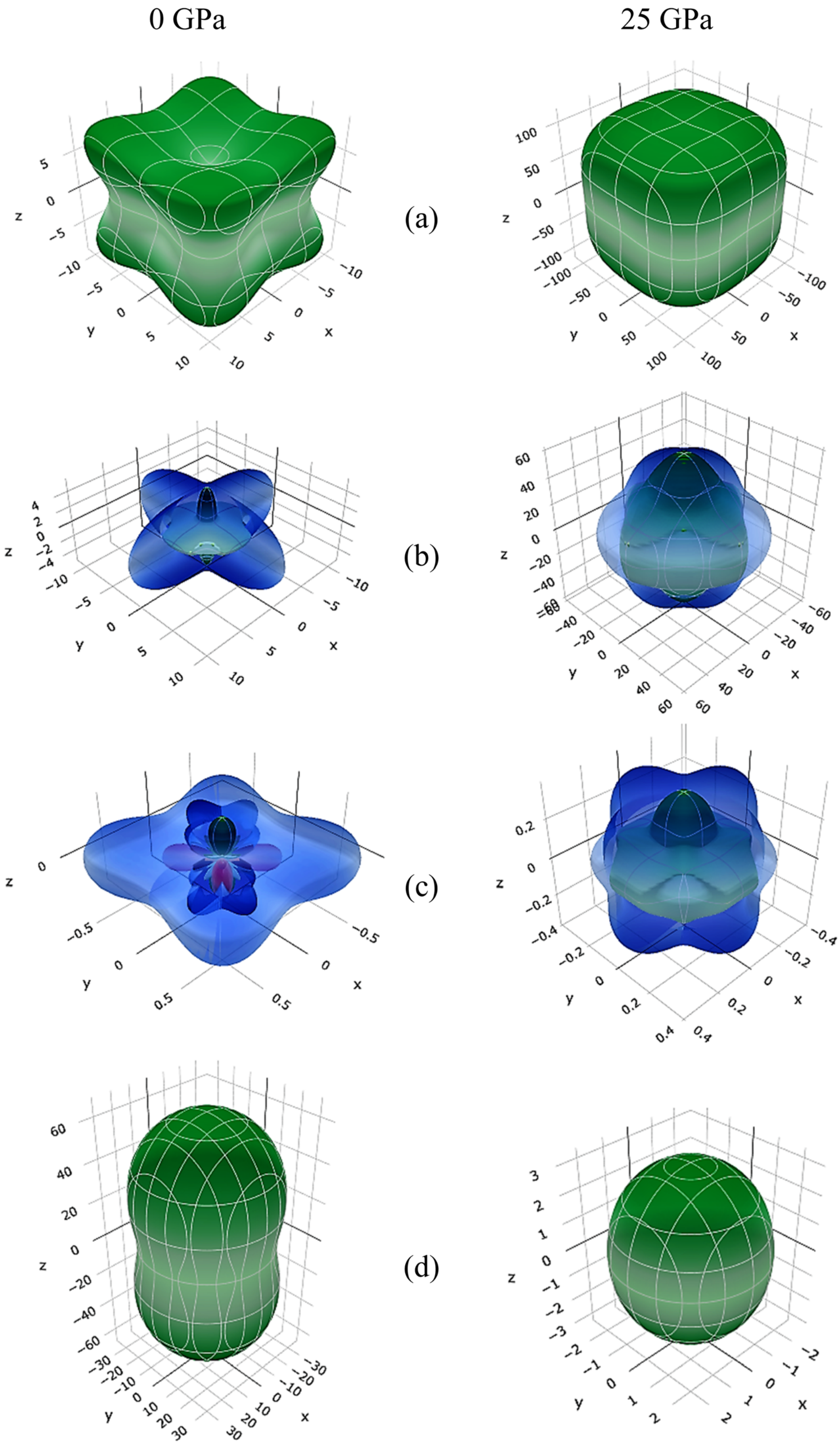

Fig. 9 Anisotropic three-dimensional depiction of (a) Young's modulus, (b) Shear modulus, and (c) Poisson's ratio (d) linear compressibility of $CsSn_2Br_5$ perovskite at 0 and 25 GPa pressures.

minimum and maximum values of Young's modulus E, linear compressibility β, Shear modulus G, and Poisson's ratio ν for both compounds are shown in Tables 1 and 2, respectively. All of these values, with the exception of β, go up as pressure is applied to KSn_2Br_5, whereas β and ν go down as pressure is applied to $CsSn_2Br_5$.

Table 1 The minimum and maximum limits of Young's modulus, E (GPa), linear compressibility, β (GPa), Shear modulus, G (GPa), and Poisson's ratio, ν of KSn_2Br_5 perovskite

	E			β			G			ν		
P (GPa)	E_{min}	E_{max}	A_E	β_{min}	β_{max}	A_β	G_{min}	G_{max}	A_G	ν_{min}	ν_{max}	A_ν
0	14.09	28.65	2.03	20.89	49.92	2.39	7.02	13.01	1.85	0.10	0.38	3.75
5	33.98	54.61	1.61	7.39	10.73	1.45	14.03	23.95	1.71	0.11	0.49	4.53
10	49.35	86.95	1.76	5.16	5.43	1.05	19.37	35.47	1.83	0.09	0.53	5.70
15	59.21	112.42	1.89	3.62	4.23	1.17	23.68	45.07	1.90	0.09	0.57	5.88
20	71.79	139.22	1.94	3.09	3.21	1.04	28.36	57.58	2.03	0.09	0.57	6.54
25	84.72	169.81	2.00	2.59	2.71	1.05	33.43	72.55	2.17	0.09	0.57	6.25

Table 2 The minimum and maximum limits of Young's modulus, E (GPa), linear compressibility, β (GPa), Shear modulus, G (GPa), and Poisson's ratio, ν of KSn_2Br_5 perovskite

	E			β			G			ν		
P (GPa)	E_{min}	E_{max}	A_E	β_{min}	β_{max}	A_β	G_{min}	G_{max}	A_G	ν_{min}	ν_{max}	A_ν
0	3.94	15.57	3.96	32.56	64.68	1.99	1.16	11.10	6.32	−0.48	1.09	∞
5	29.14	59.65	2.05	5.32	15.05	2.83	12.76	24.23	1.89	0.05	0.54	10.19
10	47.33	80.63	1.70	4.13	7.89	1.91	19.21	31.44	1.64	0.12	0.49	4.24
15	70.58	102.26	1.45	3.55	4.95	1.39	27.50	39.52	1.44	0.17	0.44	2.55
20	85.42	126.74	1.48	2.89	3.81	1.31	32.90	51.18	1.56	0.144	0.46	3.19
25	106.90	145.15	1.36	2.60	3.13	1.20	39.08	58.40	1.49	0.16	0.45	2.82

3.4 Debye temperature

The Debye temperature, denoted as Θ_D, is an essential attribute in the field of thermodynamics that is associated with the highest frequency mode of vibrations in a crystal.[64] It creates a correlation among multiple fundamental physical parameters, including specific heat, lattice stability, melting point, and thermal expansion. Debye temperature was calculated using the obtained elastic moduli for MSn_2Br_5 perovskites. In order to determine the average sound velocity ν_m within a solid, the equation employed is as follows:

$$\nu_m = \left[\frac{1}{3}\left(\frac{2}{{\nu_t}^3} + \frac{1}{{\nu_l}^3}\right)\right]^{\frac{-1}{3}} \tag{1}$$

in this context, ν_t and ν_l represent the transverse and longitudinal sound velocities, respectively. These velocities can be obtained by utilizing the values of bulk modulus (B) and shear modulus (G) in the subsequent equation:

$$\nu_t = \left(\frac{G}{\rho}\right)^{\frac{1}{2}} \tag{2}$$

and

$$\nu_l = \left(\frac{3B + 4G}{3\rho}\right)^{\frac{1}{2}} \tag{3}$$

hence,

$$\Theta_D = \frac{h}{k}\left[\frac{3n}{\pi}\left(\frac{N_A \rho}{M}\right)\right]^{\frac{1}{3}} \nu_m \tag{4}$$

in the above equation, h represents Plank's constant, k denotes Boltzmann's constant, n signifies the number of atoms in a molecule, N_A represents the Avogadro number, ρ denotes the

Table 3 The Voigt and Reuss values of C_{44}^R & C_{44}^V (in GPa), equivalent Zener anisotropic factor (A^{eq}), Shear anisotropy (A^G), bulk anisotropy (A^B), universal log-Euclidean index (A^L) Kleinman parameter (ζ), and machinability index (μ_M) of KSn_2Br_5 perovskite at various applied pressures P (GPa)

P	C_{44}^R	C_{44}^V	A^{eq}	A^U	A^G	A^B	A^L	ζ	μ_M
0	2.47	2.48	1.83	0.45	0.03	0.045	0.09	0.56	1.50
5	6.17	6.27	1.52	0.21	0.02	0.004	0.04	0.60	1.99
10	10.24	11.03	1.70	0.35	0.03	0.000	0.17	0.59	1.76
15	13.01	14.02	1.77	0.40	0.04	0.000	0.17	0.62	1.93
20	16.40	17.90	1.85	0.46	0.04	0.000	0.20	0.60	1.82
25	20.04	22.58	1.94	0.55	0.05	0.000	0.27	0.60	1.72

Table 4 : The Voigt and Reuss values of C_{44}^R & C_{44}^V (in GPa), equivalent Zener anisotropic factor (A^{eq}), Shear anisotropy (A^G), bulk anisotropy (A^B), universal log-Euclidean index (A^L) Kleinman parameter (ζ), and machinability index (μ_M) of $CsSn_2Br_5$ perovskite at various applied pressures, P (GPa)

P	C_{44}^R	C_{44}^V	A^{eq}	A^U	A^G	A^B	A^L	ζ	μ_M
0	1.97	2.11	3.91	2.59	0.20	0.01	0.15	0.52	1.47
5	6.63	7.04	1.89	0.50	0.04	0.03	0.15	0.68	1.78
10	9.51	9.75	1.64	0.30	0.03	0.01	0.06	0.69	2.03
15	12.08	12.40	1.44	0.16	0.02	0.00	0.06	0.67	2.12
20	15.41	16.04	1.50	0.20	0.02	0.00	0.09	0.67	2.04
25	17.88	18.40	1.43	0.15	0.01	0.00	0.06	0.67	2.06

Table 5 Measured density ρ (kg m^{-3}), transverse sound velocity v_t (m s^{-1}), longitudinal sound velocity v_l (m s^{-1}), mean sound velocity v_m (m s^{-1}), Debye temperature Θ_D (K) of the MSn$_2$Br$_5$ (M = K, Sn) perovskites

	KSn$_2$Br$_5$					CsSn$_2$Br$_5$				
P (GPa)	ρ (kg m^{-3})	v_t (m s^{-1})	v_l (m s^{-1})	v_m (m s^{-1})	Θ_D (K)	ρ (kg m^{-3})	v_t (m s^{-1})	v_l (m s^{-1})	v_m (m s^{-1})	Θ_D (K)
0	4257	1398.01	2299.68	1544.47	143.18	4346	1019.82	1781.73	1133.00	101.24
5	5263	1868.77	3483.26	2086.73	207.64	5565	1828.69	3417.71	2042.37	198.17
10	5795	2211.43	4158.77	2470.91	253.88	6164	2048.25	3969.59	2293.21	230.22
15	6194	2402.78	4666.47	2690.50	282.65	6601	2276.52	4418.35	2549.01	261.81
20	6531	2596.77	5007.27	2906.37	310.76	6970	2452.71	4794.58	2747.54	287.37
25	6822	2792.81	5356.22	3124.67	338.99	7287	2589.15	5042.48	2899.70	307.81

density of the solid, M represents the weight of the molecule, and v_m represents the average speed of sound in a certain medium.

Eqn (1)–(4) shows that as pressure is applied, the Debye temperature of MSn$_2$Br$_5$ perovskite rises. This leads to an increase in atomic force. Table 5 provides the expected values for pressure-dependent densities (ρ), longitudinal sound velocity (v_l), transverse sound velocity (v_t), average sound velocity (v_m), and Debye temperatures (Θ_D). The observed results demonstrate a positive correlation with the rise in pressure. Furthermore, we have encountered difficulty in locating any previous research or theoretical frameworks that have yielded similar findings to our work. Therefore, we anticipate that our discovery will help further the progress of future studies.

3.5 Electronic properties

The physical properties of solids can be deduced from their electronic band structures, which can be understood by locating electrons in the conduction and valence bands. The energy dispersion of electrons within the material is greatly influenced by their behaviour along the symmetric directions of the Brillouin zone, namely Z-G-X-P-N-G. Fig. 10 and 11 present an analysis of the electronic energy dispersion graph of the Brillouin zone for MSn$_2$Br$_5$ (M = K, Cs) perovskites at 0 GPa and 25 GPa pressures along its highly symmetric directions. The Fermi level (E_F) is depicted by the red dashed line at zero on the photon energy scale. At 0 GPa, KSn$_2$Br$_5$ exhibits a band gap of 2.423 eV, while at 25 GPa, the band gap reduces to 0.773 eV. Similarly, CsSn$_2$Br$_5$ demonstrates band gaps of 2.46 eV and 1.324 eV at 0 GPa and 25 GPa, respectively. These results indicate that both materials exhibit semiconductor behavior under the given conditions. An improved electrical conductivity may result from the pressure-induced narrowing of the band gap.

The reduced band gap leading to improved electrical conductivity opens up exciting possibilities in the field of electronics. It suggests that MSn$_2$Br$_5$ could be utilized in the development of more efficient and high-performance electronic devices, such as transistors or integrated circuits. The enhanced conductivity at high pressures may enable faster electron flow, thereby enhancing overall device performance.[65] Furthermore, the modified electronic properties of MSn$_2$Br$_5$ make it a promising candidate for catalytic applications. The increased electrical conductivity under pressure could facilitate electron transfer during catalytic reactions, resulting in improved efficiency and reactivity. This potential could be harnessed in areas such as energy conversion, chemical synthesis, and environmental remediation.

The electronic characteristics of MSn$_2$Br$_5$ were better understood by calculating its total density of states (TDOS) and partial density of states (PDOS). The computed TDOS values for KSn$_2$Br$_5$ at 0 GPa were found to be 7.88 states per eV per f.u.,

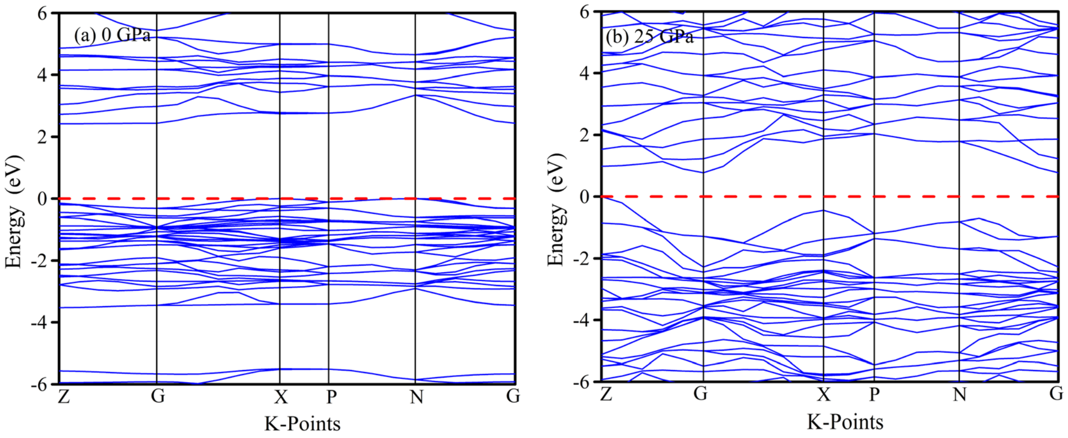

Fig. 10 Pressure effect on band structure of KSn$_2$Br$_5$ perovskite at (a) 0 and (b) 25 GPa pressures.

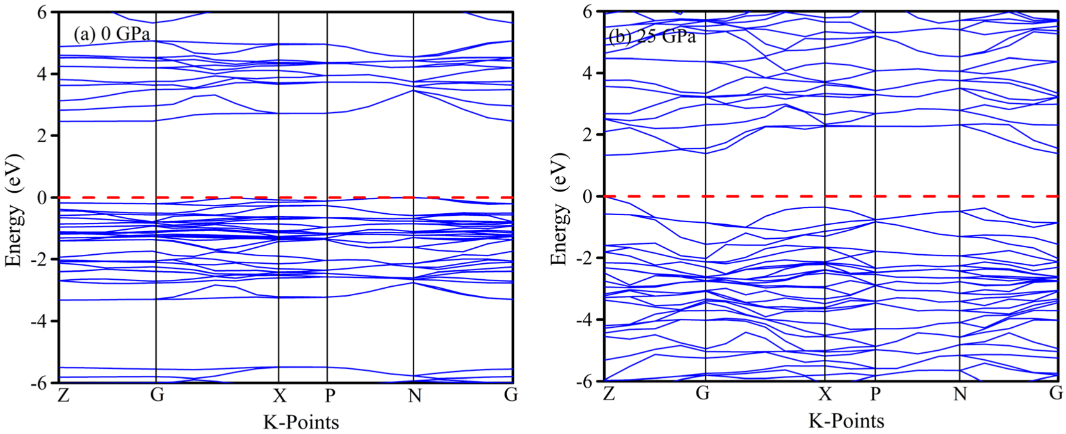

Fig. 11 Pressure effect on band structure of $CsSn_2Br_5$ perovskite at (a) 0 and (b) 25 GPa pressures.

while those for $CsSn_2Br_5$ were 8.09 states per eV per f.u. Both values dropped to 3.31 states per eV per f.u. and 4.14 states per eV per f.u. at 25 GPa. Calculated TDOS and PDOS for the MSn_2Br_5 substances at 0 and 25 GPa pressures are shown in Fig. 12. This figure provides insight into the atomic contributions to the band creation of these substances. The DOS analysis reveals the presence of n-type carriers in all the compounds, as evidenced by the high peak for electron crossings at E_F.[66]

In the case of KSn_2Br_5, the states of K, Sn, and Br play a primary role in the production of the partial density of states (PDOS) in the valence band near the Fermi level (E_F). At 0 GPa, the PDOS values for K, Sn, and Br at E_F are approximately 0.07 states per eV per f.u., 0.28 states per eV per f.u., and 2.85 states per eV per f.u., respectively. At 25 GPa, these values increase to approximately 0.61 states per eV per f.u. and 6.86 states per eV per f.u. for Sn and Br, respectively. However, the PDOS value for K does not vary considerably with increasing pressure. These findings demonstrate that Br atoms have the largest role in the production of PDOS close to E_F. The energy of the Br-4p states strongly influences the valence band between −1.89 eV and

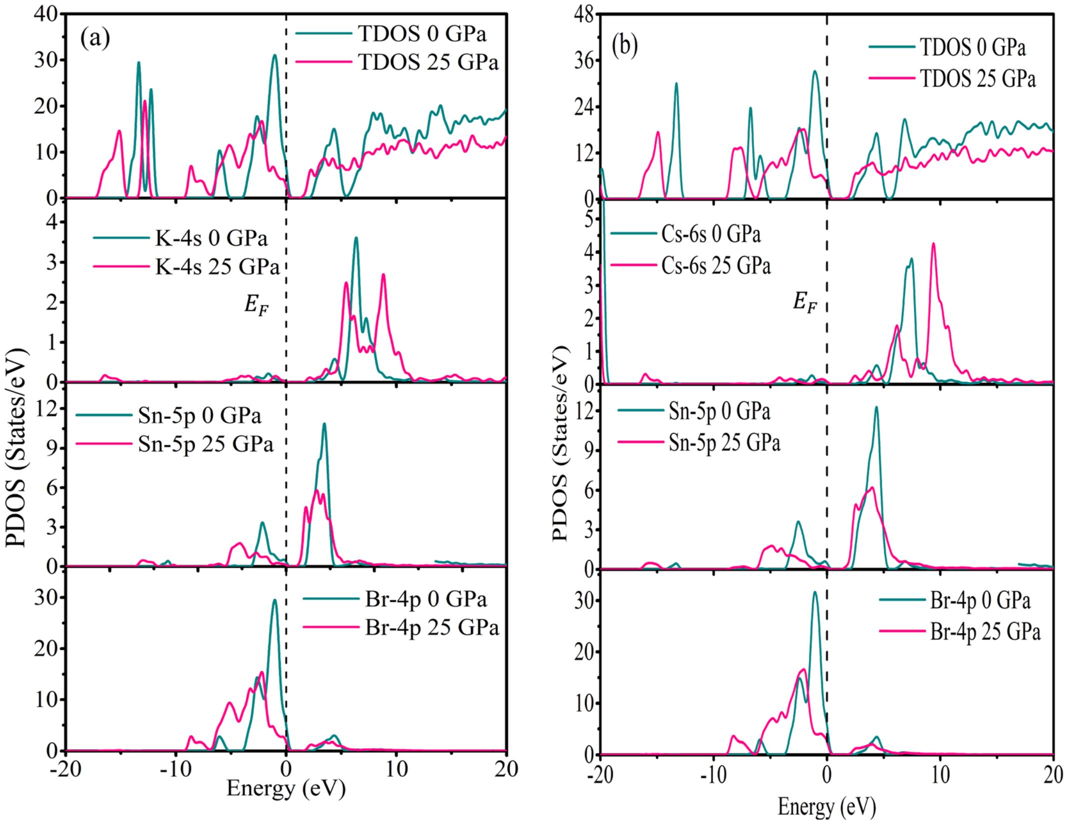

Fig. 12 (a) TDOS and PDOS of KSn_2Br_5 and (b) TDOS and PDOS of $CsSn_2Br_5$ perovskites under pressure.

−0.29 eV. The hybridization of Br-4p states has a important effect on the valence band close to E_F, which spans from −0.27 eV to −3.68 eV. For $CsSn_2Br_5$, at 0 GPa, the Cs-6s states have a negligible effect near E_F, while the Br-4p states make a high contribution at that pressure. At 25 GPa, the PDOS values for Br in both compounds exhibit a significant effect, indicating a modification in its electronic contribution. This alteration can be attributed to changes in the bonding environment or electronic interactions within the material under high pressure. These results indicate that the electronic states of the Br atom are pressure-sensitive and undergo a significant change under these conditions.

3.6 Optical properties

Information about a substance can be gathered from its optical characteristics, especially when combined with optoelectronic devices. It is of the greatest significance to do research into the reaction of different materials to electromagnetic radiation. The optical properties are investigated by monitoring the variations in response to varying incident photon energies.

The absorption coefficient is a measure of the extent to which a material absorbs light as it passes through. A small absorption coefficient implies that the material allows more radiation to pass through, while a larger coefficient indicates greater light absorption. In the case of MSn_2Br_5 (M = K, Cs) perovskites, their absorption characteristics are depicted in Fig. 13(a) and 14(a). The absorption process begins at energy levels of 1.32 eV and 1.40 eV for KSn_2Br_5 and $CsSn_2Br_5$, respectively. As the photon energy increases, the optical absorption also increases, reaching maximum values of approximately 13.03 eV for KSn_2Br_5 and 12.63 eV for $CsSn_2Br_5$. An interesting observation is that the absorption spectra of these perovskite materials exhibit a blue shift for photon energies equal to or greater than 5.22 eV and 5.34 eV. This blue shift signifies a reduction in the material's bandgap energy, enabling them to absorb photons with higher energies. However, beyond these specific peaks, the efficiency of absorption gradually diminishes for higher energy photons.

The reflectivity curve has the greatest significance in assessing the appropriateness of an element as a reflector. Fig. 13(b) and 14(b) depict the pressure-induced reflectivity spectrum of the MSn_2Br_5 (M = K, Cs) material, covering photon energies up to 30 eV. In case of KSn_2Br_5, the reflectivity begins with a value of zero photon energy and gradually increases as the incident photon energy rises. It reaches its peak value at approximately 4.41 eV and then remains relatively constant in the ultraviolet (UV) range, specifically between 6 and 15 eV. Beyond 27 eV, the reflectivity decreases and eventually reaches zero. For $CsSn_2Br_5$, the maximum reflectivity occurs at a photon energy of 4.83 eV. From there, it decreases significantly and reaches its minimum at approximately 24.58 eV. The reflectance remains constant within the ultraviolet spectrum, specifically

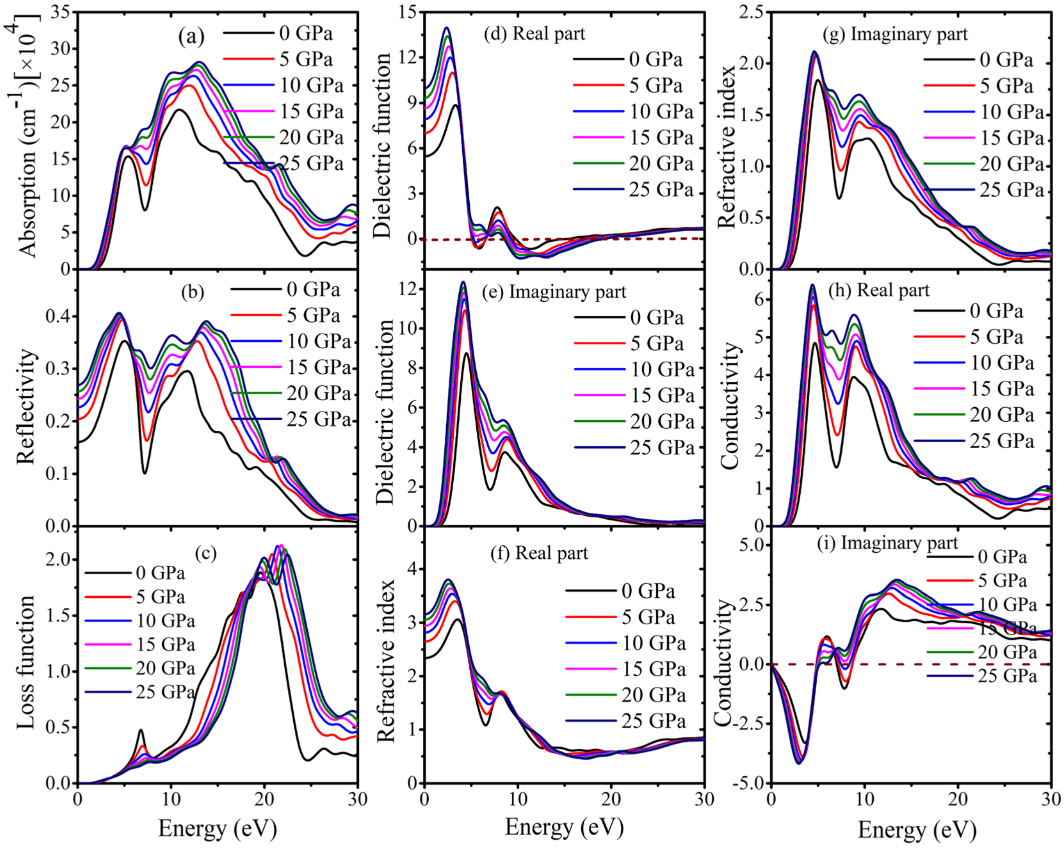

Fig. 13 (a) Absorption (b) reflectivity (c) loss function (d and e) dielectric function (f and g) refractive index (h and i) conductivity of KSn_2Br_5 perovskite in [100] direction as a function of pressure.

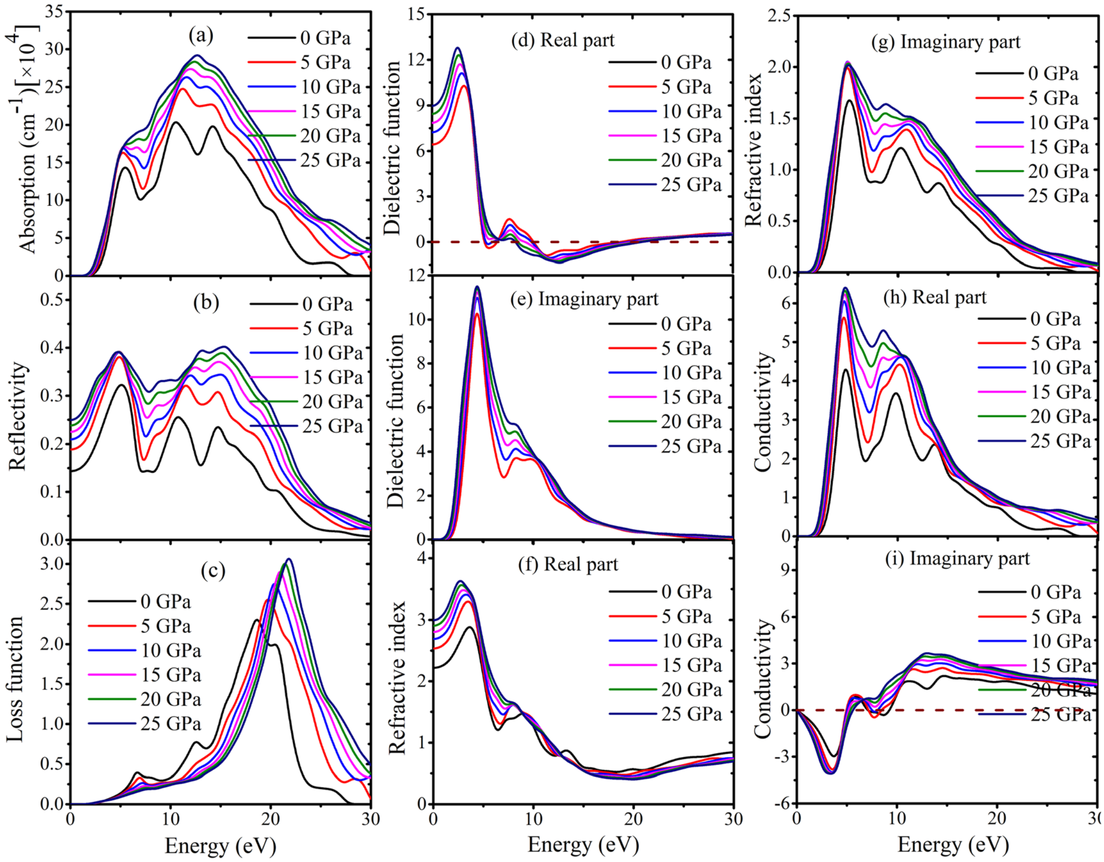

Fig. 14 (a) Absorption (b) reflectivity (c) loss function (d and e) dielectric function (f and g) refractive index (h and i) conductivity of $CsSn_2Br_5$ perovskite in [100] direction as a function of pressure.

from 25 to 30 eV. Based on these observations, it can be concluded that MSn_2Br_5 (M = K, Cs) can serve as an effective reflector across the entire ultraviolet light spectrum.

The loss function quantifies the amount of energy dissipated by an electron during its passage through a given substance.[67] Fig. 13(c) and 14(c) show the loss function curves for MSn_2Br_5 (M = K, Cs) compounds. The loss function is closely connected to the phenomenon of plasma oscillation and its corresponding frequency, known as the plasma frequency (ω_p).[68] We found that for KSn_2Br_5, the highest loss function is 21.84 eV at 15 GPa. At 25 GPa, the highest loss function for $CsSn_2Br_5$ is 21.88 eV. These observations yield an approximation of the plasma frequency of MSn_2Br_5 molecules. When the incident light frequency exceeds the plasma frequency, the materials MSn_2Br_5 exhibit transparency. This phenomenon arises due to the inability of the electrons within the material to effectively assimilate the energy carried by the incident light. The optical characteristics of a metallic system transition from metallic to dielectric-like beyond the plasma energy.[69] The loss function's peak undergoes a shift towards larger energy values as the pressure is increased. The decrease in the number of effective electrons engaging in intraband and interband transitions is observed as the peak shifts towards higher energies.[70] This is because the applied pressure compresses the material, reducing the number of available states for the electrons to occupy.

In comparison to radiation, the dielectric function shows how the permittivity of a material changes with frequency or distance. The dielectric functions for the perovskite compounds MSn_2Br_5 (M = K, Cs) are illustrated in Fig. 13(d), (e), 14(d) and (e). These figures display the real and imaginary components of the dielectric functions at different pressures, covering a range of photon energies up to 30 eV. The dielectric function of KSn_2Br_5 demonstrates a peak value of around ∼14.01 at a photon energy of 2.33 eV, after which it steadily drops as the photon energy increases. In the case of $CsSn_2Br_5$, it has been observed that the maximum recorded dielectric constant value is around 12.79 (real) with an incident photon energy of 2.55 eV. Furthermore, it has been noted that the dielectric constant falls as the incident photon energy increases. Nevertheless, in the high-energy region, the real and imaginary components exhibit a tendency to converge towards zero for both substances. The behavior of MSn_2Br_5 in this particular region exhibits similarities to that of other transparent materials. It is worth noting that the dielectric characteristics of MSn_2Br_5 exhibit negligible changes when subjected to external forces. The dielectric characteristics of the material exhibit minimal alteration when subjected to external pressure. The observed pressure-invariant behavior is particularly remarkable throughout the high-energy region, since the real and imaginary components of the dielectric function tend to converge towards zero. As a result, the optical absorption profile, which is strongly linked to the imaginary component of the dielectric function, has minimal alterations as a consequence of pressure influences.[71] The aforementioned results underscore the strong and enduring dielectric characteristics exhibited by compounds of MSn_2Br_5, as well as their limited vulnerability to alterations generated by pressure.

The refractive index of a substance is an intrinsic characteristic that delineates the manner in which light behaves when it traverses the substance. This observation yields significant revelations regarding the velocity of light propagation within the given substance. The phase velocity of light is determined by the real portion of the refractive index, whereas the imaginary part of the refractive index corresponds to the extinction coefficient. The extinction coefficient signifies the material's capacity to dissipate energy prior to total absorption. The investigation of the refractive index's real and imaginary components has been conducted for the perovskite materials MSn_2Br_5 (M = K, Cs). Fig. 13(f), (g), 14(f) and (g) illustrate the behavior of these components at zero photon energy. The analysis reveals that the real component of the refractive index reaches a maximum value of approximately 2.55 eV for KSn_2Br_5 and 2.65 eV for $CsSn_2Br_5$. As the energy increases above this values, the real component gradually decreases and eventually reaches a minimum value of about 13.77 eV and 14.98 eV for KSn_2Br_5 and $CsSn_2Br_5$, respectively. In the upper energy range, the real component remains relatively constant. This behavior signifies changes in the phase velocity of light within the material's and suggests a shift in their optical response at higher energies.

In relation to the imaginary component of the refractive index, the values exhibit a rising pattern and reach their peak at around 4.65 eV and 4.96 eV for the compounds KSn_2Br_5 and $CsSn_2Br_5$, respectively. As the energy increases, these values exhibit gradual decreases and eventually stabilize in the higher energy range. As a result of these findings, we may deduce that the material has good absorption properties and a high rate of energy dissipation. Fig. 13(h), (i), 14(h) and (i) illustrate pressure-dependent changes in the optical conductivity of MSn_2Br_5 (M = K, Cs) compounds for light with energy up to 30 eV. Spectral analysis of optical photoconductivity exhibits distinct patterns within the studied energy range. Both KSn_2Br_5 and $CsSn_2Br_5$ compounds demonstrate a maximum conductivity at energies 4.41 eV and 4.72 eV, respectively. With increasing photon energy beyond these values, the conductivity transitions to higher energy regions under external pressure. Subsequently, with increasing photon energy, conductivity falls progressively and approaches a minimum. The imaginary part of the conductivity also exhibits this behavior when exposed to incident radiation, flattening out at higher energy. Based on these results, it appears that absorbing light increased the photoconductivity of MSn_2Br_5 (M = K, Cs) materials.

4. Conclusion

First principles DFT-based simulations were used to explore the physical properties of the non-toxic perovskite compounds MSn_2Br_5 (M = K, Cs) at various pressures up to 25 GPa. It works on different kinds of physical properties, such as structural, elastic, mechanical, Debye temperatures, electronic, and optical. At normal pressure, the calculated lattice parameters agreed with the experimental results. But the values of the lattice constants and unit cell volume also dropped with increasing pressure because of the smaller interatomic distances. When subjected to external pressure, the strength of the ionic/covalent/metallic bonds inside the compounds increased. MSn_2Br_5 perovskites were mechanically stable, and their elastic constants increased with applied pressures, indicating increased rigidity and deformation resistance. The anisotropy values of E, β, G, and ν in MSn_2Br_5 (M = K, Cs) perovskites revealed the presence of elastic anisotropy in all directions. Elastic anisotropy was determined in all directions by measuring the anisotropy parameters E, β, G, and ν in MSn_2Br_5 (M = K, Cs) perovskites. Notably, with rising pressure, the values of E, G, and ν generally increased in KSn_2Br_5, while β and ν decreased in $CsSn_2Br_5$. The obtained results provide valuable insights into the mechanical behaviour and anisotropic characteristics exhibited by the examined perovskite compounds. Moreover, under pressure, the Debye temperature of the perovskites increased, indicating stronger atomic forces. This enhancement in conductivity at high pressures could improve device performance and be beneficial in wide range of uses, for example energy conversion, chemical synthesis, and environmental remediation. Further, the results of this research also provided valuable insights into the electronic properties of the compounds, indicating that they exhibit semiconducting behavior under the given conditions. The band gaps decreased with increasing pressure, allowing for enhanced electrical conductivity. The density of states (DOS) revealed atomic electronic contributions. It was found that pressure influenced the electronic states associated with the Br atoms significantly. Additionally, the compounds showed potential as effective reflectors across the entire UV spectrum and exhibited pressure-stable dielectric properties. The refractive index indicated changes in light's phase velocity, and optical conductivity revealed enhanced photoconductivity through photon absorption. These findings contribute to the understanding and utilization of MSn_2Br_5 compounds in energy, catalysis, and environmental applications. Finally, these results have a major influence on the future of perovskite solar cell technology and its widespread application in renewable energy systems.

Conflicts of interest

The authors state that to the best of their knowledge, they have no financial or personal affiliations that may be construed as having influenced the work disclosed in this paper.

Acknowledgements

The authors acknowledge some financial support for this study from Pabna University of Science and Technology, Bangladesh.

References

1 T. C. Jellicoe, J. M. Richter, H. F. J. Glass, M. Tabachnyk, R. Brady, S. E. Dutton, A. Rao, R. H. Friend, D. Credgington, N. C. Greenham and M. L. Böhm, Synthesis and optical properties of lead-free cesium tin halide perovskite nanocrystals, *J. Am. Chem. Soc.*, 2016, **138**, 2941–2944.

2 A. Bernasconi, A. Rizzo, A. Listorti, A. Mahata, E. Mosconi, F. De Angelis and L. Malavasi, Synthesis, properties, and modeling of Cs1−xRbxSnBr3 solid solution: a new mixed-cation lead-free all-inorganic perovskite system, *Chem. Mater.*, 2019, **31**, 3527–3533.

3 O. V. Oyelade, O. K. Oyewole, D. O. Oyewole, S. A. Adeniji, R. Ichwani, D. M. Sanni and W. O. Soboyejo, Pressure-assisted fabrication of perovskite solarcells, *Sci. Rep.*, 2020, **10**, 7183.

4 R. Nie, R. R. Sumukam, S. H. Reddy, M. Banavoth and S. I. Seok, Lead-free perovskite solar cells enabled by hetero-valent substitutes, *Energy Environ. Sci.*, 2020, **13**, 2363–2385.

5 M. Llanos, R. Yekani, G. P. Demopoulos and N. Basu, Alternatives assessment of perovskite solar cell materials and their methods of fabrication, *Renewable Sustainable Energy Rev.*, 2020, **133**, 110207.

6 Z. Lan, J. Meng, K. Zheng and I. E. Castelli, Exploring the intrinsic point defects in cesium copper halides, *J. Phys. Chem. C*, 2021, **125**, 1592–1598.

7 D. Moghe, L. Wang, C. J. Traverse, A. Redoute, M. Sponseller, P. R. Brown, V. Bulović and R. R. Lunt, All vapor-deposited lead-free doped CsSnBr3 planar solar cells, *Nano Energy*, 2016, **28**, 469–474.

8 S. J. Clark, C. D. Flint and J. D. Donaldson, Luminescence and electrical conductivity of CsSnBr3, and related phases, *J. Phys. Chem. Solids*, 1981, **42**, 133–135.

9 J. C. Zheng, C. H. A. Huan, A. T. S. Wee and M. H. Kuok, Electronic properties of CsSnBr3: studies by experiment and theory, *Surf. Interface Anal.*, 1999, **28**, 81–83.

10 M. L. Ali, M. K. Alam, M. Khan, M. N. M. Nobin, N. Islam, U. Faruk and M. Z. Rahaman, Pressure-dependent structural, electronic, optical, and mechanical properties of superconductor CeRh2As2: A first-principles study, *Phys. B*, 2023, **668**, 414224.

11 M. Saiduzzaman, T. Takei and N. Kumada, Hydrothermal magic for the synthesis of new bismuth oxides, *Inorg. Chem. Front.*, 2021, **8**, 2918–2938.

12 M. L. Ali, M. Khan, M. A. Asad and M. Z. Rahaman, Highly efficient and stable lead-free Cesium Copper halide perovskite for optoelectronic applications: A DFT based study, *Haliyon*, 2023, **9**, e18816.

13 M. Khan, M. R. Hossain and M. L. Ali, Pressure-induced physical properties in topological semi-metals MAS2 (M = Hf, Ti), *Results Phys.*, 2023, **52**, 106860.

14 A. S. Bhalla, R. Guo and R. Roy, The perovskite structure—a review of its role in ceramic science and technology, *Mater. Res. Innovations*, 2000, **4**, 3–26.

15 P. Kanhere and Z. Chen, A review on visible light active perovskite-based photocatalysts, *Molecules*, 2014, **19**, 19995–20022.

16 A. N. Baranov, D. C. Kim, J. S. Kim, H. R. Kang, Y. W. Park, J. S. Pshirkov and E. V. Antipov, Superconductivity in the Ba1−xKxBiO3 system, *Phys. C*, 2001, **357**, 414–417.

17 W. Dong, B. Li, Y. Li, X. Wang, L. An, C. Li, B. Chen, G. Wang and Z. Shi, General approach to well-defined perovskite MTiO3 (M= Ba, Sr, Ca, and Mg) nanostructures, *J. Phys. Chem. C*, 2011, **115**, 3918–3925.

18 V. V. Lemanov, A. V. Sotnikov, E. P. Smirnova, M. Weihnacht and R. Kunze, Perovskite CaTiO3 as an incipient ferroelectric, *Solid State Commun.*, 1999, **110**, 611–614.

19 J. Jia, S. Guo, S. Yan, F. Cao, C. Yao, X. Dong and G. Wang, Simultaneous large pyroelectric response and high depolarization temperature in sodium bismuth titanate-based perovskites, *Appl. Phys. Lett.*, 2019, **114**, 032902.

20 N. H. Linh, N. H. Tuan, D. D. Dung, P. Q. Bao, B. T. Cong and L. T. H. Thanh, Alkali metal-substituted bismuth-based perovskite compounds: a DFT study, *J. Sci.: Adv. Mater. Devices*, 2019, **4**, 492–498.

21 G. Murtaza, I. Ahmad and A. Afaq, Shift of indirect to direct bandgap in going from K to Cs in MCaF3 (M= K, Rb, Cs), *Solid State Sci.*, 2013, **16**, 152–157.

22 S. S. A. Gillani, R. Ahmad, M. Rizwan, M. Rafique, G. Ullah, C. B. Cao and H. B. Jin, Effect of magnesium doping on band gap and optical properties of SrZrO3 perovskite: a first-principles study, *Optik*, 2019, **191**, 132–138.

23 S. S. A. Gillani, R. Ahmad, I. Zeba, I. u-din, M. Rizwan, M. Rafique, M. Shakil, S. Jabbar and M. Siddique, Structural stability of SrZrO3 perovskite and improvement in electronic and optical properties by Ca and Ba doping for optoelectronic applications: a DFT approach, *Philos. Mag. Lett.*, 2019, **99**, 3133–3145.

24 N. A. Noor, M. Rashid, S. M. A. Abbas, M. Raza, A. Mahmood, S. M. Ramay and G. Murtaza, Shift of indirect to direct bandgap and thermoelectric response of the cubic BiScO3 via DFT-mBJ studies, *Mater. Sci. Semicond. Process.*, 2016, **49**, 40–47.

25 J. Islam and A. A. Hossain, Semiconducting to metallic transition with outstanding optoelectronic properties of CsSnCl3 perovskite under pressure, *Sci. Rep.*, 2020, **10**, 14391.

26 S. Zhang, L. Zhang, Q. Tian, X. Gu, Y. Du, K. Zhao and S. Liu, Spontaneous construction of multidimensional heterostructure enables enhanced hole extraction for inorganic perovskite solar cells to exceed 20% efficiency, *Adv. Energy Mater.*, 2022, **12**, 2103007.

27 N. K. Noel, S. D. Stranks, A. Abate, C. Wehrenfennig, S. Guarnera, A.-A. Haghighirad, A. Sadhanala, G. E. Eperon, S. K. Pathak and M. B. Johnston, Lead-free organic–inorganic tin halide perovskites for photovoltaic applications, *Energy Environ. Sci.*, 2014, **7**, 3061.

28 P. K. Rahul, R. Singh, V. Singh, B. Bhattacharya and Z. H. Khan, New class of lead free perovskite material for low-cost solar cell application, *Mater. Res. Bull.*, 2018, **97**, 572.

29 R. Mosca, P. Ferro, T. Besagni, D. Calestani, F. Chiarella and F. Licci, Effect of humidity on the ac impedance of CH3NH3SnCl3 hybrid films, *Appl. Phys. A*, 2011, **104**, 1181.

30 Y. Chen, M. S. Molokeev, V. V. Atuchin, A. H. Reshak, S. Auluck, Z. A. Alahmed and Z. Xia, Synthesis, crystal structure, and optical gap of two-dimensional halide solid solutions CsPb2(Cl1−xBrx)5, *Inorg. Chem.*, 2018, **57**, 9531.

31 P. Acharyya, P. Pal, P. K. Samanta, A. Sarkar, S. K. Pati and K. Biswas, Single pot synthesis of indirect band gap 2D CsPb2Br5 nanosheets from direct band gap 3D CsPb2Br3 nanocrystals and the origin of their luminescence properties, *Nanoscale*, 2019, **11**, 4001.

32 K.-H. Wang, L. Wu, L. Li, H.-B. Yao, H.-S. Qian and S.-H. Yu, Large-scale synthesis of highly luminescent perovskite-related CsPb2Br5 nanoplatelets and their fast anion exchange, *Angew. Chem., Int. Ed.*, 2016, **55**, 8328.

33 L. Ruan, J. Lin, W. Shen and Z. Deng, Ligand-mediated synthesis of compositionally related cesium lead halide CsPb2X5 nanowires with improved stability, *Nanoscale*, 2018, **10**, 7658.

34 X. Tang, Z. Hu, W. Yuan, W. Hu, H. Shao, D. Han, J. Zheng, J. Hao, Z. Zang, J. Du, Y. Leng, L. Fang and M. Zhou, Perovskite CsPb2Br5 microplate laser with enhanced stability and tunable properties, *Adv. Opt. Mater.*, 2017, **5**, 1600788.

35 I. Abrahams, D. Z. Demetriou, R. T. Kroemer, H. Taylor and M. Motevalli, Evidence for cluster orbital formation in CsPb2X5 compounds (X = Cl, Br), *J. Solid State Chem.*, 2001, **160**, 382.

36 S. Bonomi, M. Patrini, G. Bongiovanni and L. Malavasi, Versatile vapor phase deposition approach to cesium tin bromide materials CsPb2Br3, CsPb2Br5and CsPb2Br6, *RSC Adv.*, 2020, **10**, 28478.

37 K. Nasyedkin, I. King, L. Zhang, P. Chen, L. Wang, R. J. Staples, R. R. Lunt and J. Pollanen, Extraordinary phase coherence length in epitaxial halide perovskites, *iScience*, 2021, **24**, 102912.

38 S. J. Clark, *et al.*, Kristallogr, First principles methods using CASTEP, *Z. Kristallogr. – Cryst. Mater.*, 2005, **220**, 567.

39 M. D. Segall, *et al.*, First-principles simulation: ideas, illustrations and the CASTEP code, *J. Phys.: Condens.Matter*, 2002, **14**, 2717–2744.

40 J. P. Perdew, K. Burke and M. Ernzerhof, Generalized gradient approximation made simple, *Phys. Rev. Lett.*, 1996, **77**, 3865.

41 H. J. Monkhorst and J. D. Pack, Special points for Brillouin-zone integrations, *Phys. Rev. B: Solid State*, 1976, **13**, 5188.

42 T. H. Fischer and J. Almlof, General methods for geometry and wave function optimization, *J. Phys. Chem.*, 1952, **96**, 9768.

43 K. Momma and F. Izumi, VESTA 3 for three-dimensional visualization of crystal, volumetric and morphology data, *J. Appl. Crystallogr.*, 2011, **44**, 1272–1276.

44 R. Golesorkhtabar, P. Pavone, J. Spitaler, P. Puschnig and C. Draxl, ElaStic: A tool for calculating second-order elastic constants from first principles, *Comput. Phys. Commun.*, 2013, **184**, 1861–1873.

45 Md. L. Ali, M. M. BillaH, M. Khan, M. N. M. Nobin and M. Z. Rahaman, Pressure-induced physical properties of alkali metal chlorides Rb2NbCl6*:* A density functional theory study, *AIP Adv.*, 2023, **13**, 065110.

46 D. Becker and H. P. Beck, High Pressure Study of NH4Pb2Br5 Type Compounds. I structural parameters and their evolution under high pressure, *Z. Anorg. Allg. Chem.*, 2004, **630**, 1924–1932.

47 I. Abrahams, *et al.*, Evidence for cluster orbital formation in CsSnX5 compounds (X= Cl, Br), *J. Solid State Chem.*, 2001, **160**, 382–387.

48 H. Shi, R. Asahi and C. Stampft, Properties of the gold oxides Au_2O_3 and Au_2O: First-principles investigation, *Phys. Rev. B: Condens. Matter Mater. Phys.*, 2007, **75**, 205125.

49 Y. Pan and E. Yu, Theoretical prediction of structure, electronic and optical properties of VH2 hydrogen storage material, *Int. J. Hydrogen Energy*, 2022, **47**, 27608–27616.

50 C. Li, X. Lu, W. Ding, L. Feng, Y. Gao and Z. Guo, Formability of ABX_3 (X = F, Cl, Br, I) halide perovskites, *Acta Crystallogr. B*, 2008, **64**, 702.

51 R. Akter, M. Khan, M. N. M. Nobin, M. S. Ali, M. M. Hossain, M. Z. Rahaman and M. L. Ali, Effects of grain boundary and chemical short-range order on mechanical properties of NiCoCr multi-principal element alloys: A molecular dynamics simulations, *Mater. Today Commun.*, 2023, **36**, 106630.

52 L. Fast, *et al.*, Elastic constants of hexagonal transition metals: Theory, *Phys. Rev. B: Condens. Matter Mater. Phys.*, 1995, **51**, 17431.

53 S. Piskunov, *et al.*, Bulk properties and electronic structure of SrTiO3, BaTiO3, PbTiO3 perovskites: an ab initio HF/DFT study, *Comput. Mater. Sci.*, 2004, **29**, 165.

54 D. H. Chung and W. R. Buessem, The Voigt-Reuss-Hill (VRH) approximation and the elastic moduli of polycrystalline ZnO, TiO2 (Rutile), and α-Al2O3, *J. Appl. Phys.*, 1968, **39**, 2777–2782.

55 P. Ravindran, L. Fast, P. A. Korzhavyi, B. Johansson, J. Wills and O. Eriksson, Density functional theory for calculation of elastic properties of orthorhombic crystals: Application to TiSi2, *J. Appl. Phys.*, 1998, **84**, 4891–4904.

56 J. R. Xiao, B. A. Gama and J. W. Gillespie Jr, An analytical molecular structural mechanics model for the mechanical properties of carbon nanotubes, *Int. J. Solids Struct.*, 2005, **42**, 3075–3092.

57 O. N. Senkov and D. B. Miracle, Generalization of intrinsic ductile-to-brittle criteria by Pugh and Pettifor for materials with a cubic crystal structure, *Sci. Rep.*, 2021, **11**, 4531.

58 E. Mazhnik and A. R. Oganov, A model of hardness and fracture toughness of solids, *J. Appl. Phys.*, 2019, **126**, 0021–8979.

59 M. I. Naher and S. H. Naqib, Possible applications of MO2C in the orthorhombic and hexagonal phases explored via ab-initio investigations of elastic, bonding, optoelectronic and thermophysical properties, *Results Phys.*, 2022, **37**, 105505.

60 B. Fadila, M. Ameri, D. Bensaid, M. Noureddine, I. Ameri, S. Mesbah and Y. Al-Douri, Structural, magnetic, electronic and mechanical properties of full-Heusler alloys Co2YAl

(Y= Fe, Ti): first principles calculations with different exchange–correlation potentials, *J. Magn. Magn. Mater.*, 2018, **448**, 208–220.

61 Z. Sun, D. Music, R. Ahuja and J. M. Schneider, Theoretical investigation of the bonding and elastic properties of nanolayered ternary nitrides, *Phys. Rev. B: Condens. Matter Mater. Phys.*, 2005, **71**, 193402.

62 R. Gaillac, P. Pullumbi and F. X. Coudert, ELATE: an open-source online application for analysis and visualization of elastic tensors, *J. Phys.: Condens.Matter*, 2016, **28**, 275201.

63 A. Biswas, M. S. Alam, A. Sultana, T. Ahmed, M. Saiduzzaman and K. M. Hossain, Effects of Bi and Mn codoping on the physical properties of barium titanate: investigation via DFT method, *Appl. Phys. A*, 2021, **127**, 939.

64 L. Qi, Y. Jin, Y. Zhao, X. Yang, H. Zhao and P. Han, The structural, elastic, electronic properties and Debye temperature of Ni3Mo under pressure from first-principles, *J. Alloys Compd.*, 2015, **621**, 383.

65 J. Maumus, N. Bagdassarov and H. Schmeling, Electrical conductivity and partial melting of mafic rocks under pressure, *Geochim. Cosmochim. Acta*, 2005, **69**, 4703–4718.

66 N. P. Armitage, P. Fournier and R. L. Greene, Progress and perspectives on electron-doped cuprates, *Rev. Mod. Phys.*, 2010, **82**, 2421.

67 S. Boucetta, Theoretical study of elastic, mechanical and thermodynamic properties of MgRh intermetallic compound, *J. Magnesium Alloys*, 2014, **2**, 59–63.

68 S. Huang, R. Z. Li, S. T. Qi, B. Chen and J. Shen, A theoretical study of the elastic and thermal properties of *ScRu* compound under pressure, *Phys. Scr.*, 2014, **89**, 065702.

69 S. F. Pugh, XCII. Relations between the elastic moduli and the plastic properties of polycrystalline pure metals, *London, Edinburgh Dublin Philos. Mag. J. Sci.*, 1954, **45**, 823–843.

70 Y. Pan, S. Chen and Y. Lin, Vacancy-induced elastic properties and hardness of CrB4: A DFT calculation, *Int. J. Mod. Phys. B*, 2017, **31**, 1750096.

71 R. Hill, The elastic behaviour of a crystalline aggregate, *Proc. Phys. Soc., London, Sect. A*, 1952, **65**, 349.